

Article

A Comparative Study on the Vertical Structures and Microphysical Properties of a Mixed Precipitation Process over Different Topographic Positions of the Liupan Mountains in Northwest China

Ying He ¹, Zhiliang Shu ^{2,3,*} , Jiafeng Zheng ^{4,*} , Xingcan Jia ^{5,*}, Yujun Qiu ¹, Peiyun Deng ², Xue Yan ¹, Tong Lin ², Zhangli Dang ² and Chunsong Lu ¹

- ¹ China Meteorological Administration Aerosol-Cloud-Precipitation Key Laboratory, School of Atmospheric Physics, Nanjing University of Information Science and Technology, Nanjing 210044, China
 - ² Key Laboratory for Meteorological Disaster Monitoring and Early Warning and Risk Management of Characteristic Agriculture in Arid Regions, China Meteorological Administration, Yinchuan 750002, China
 - ³ Ningxia Meteorological Disaster Prevention Technology Center, Yinchuan 750002, China
 - ⁴ Plateau Atmosphere and Environment Key Laboratory of Sichuan Province, School of Atmospheric Sciences, Chengdu University of Information Technology, Chengdu 610225, China
 - ⁵ Institute of Urban Meteorology, Chinese Meteorological Administration, Beijing 100081, China
- * Correspondence: 8633204@163.com (Z.S.); zjf1988@cuit.edu.cn (J.Z.); xcjia@ium.cn (X.J.); Tel.: +86-028-8596-6389 (J.Z.)



Citation: He, Y.; Shu, Z.; Zheng, J.; Jia, X.; Qiu, Y.; Deng, P.; Yan, X.; Lin, T.; Dang, Z.; Lu, C. A Comparative Study on the Vertical Structures and Microphysical Properties of a Mixed Precipitation Process over Different Topographic Positions of the Liupan Mountains in Northwest China. *Atmosphere* **2023**, *14*, 44. <https://doi.org/10.3390/atmos14010044>

Academic Editors: Xiaoming Shi, Berry Wen and Lisa Milani

Received: 13 November 2022

Revised: 19 December 2022

Accepted: 23 December 2022

Published: 26 December 2022



Copyright: © 2022 by the authors. Licensee MDPI, Basel, Switzerland. This article is an open access article distributed under the terms and conditions of the Creative Commons Attribution (CC BY) license (<https://creativecommons.org/licenses/by/4.0/>).

Abstract: A field campaign in Liupan Mountains was carried out by the Weather Modification Center of the China Meteorological Administration to study the impact of terrain on precipitation in Northwest China. The vertical structures and microphysical characteristics of a mixed cloud and precipitation process, which means stratiform clouds with embedded convection, over three topographic positions of the Liupan Mountains, namely, the Longde (LD, located on the windward slope), Liupan (LP, located on the mountain top), and Dawan sites (DW, located on the leeward slope), are compared using measurements from ground-based cloud radar (CR), micro rain radar (MRR), and disdrometer (OTT). The 17 h process is classified into cumulus mixed (1149 min), shallow (528 min), and stratiform (570 min) cloud and precipitation stages. Among them, the vertical structures over the three sites are relatively similar in the third stage, while the differences, mainly in cloud-top heights (CTHs) and rain rates (R_s), are significant in the second stage due to the strong instability. Overall, the characteristics of higher concentrations and smaller diameters of raindrops are found in this study, especially at the LP site. Topographic forcing makes the microphysical and dynamic processes of mountaintop clouds and precipitation more intense. The updrafts are the strongest at the LP, caused by orographic uplifting, and the DW is dominated by the downdrafts due to the topography impact on the dynamic structure. Meanwhile, particle falling velocities (V_{fs}) and downdrafts rapidly increase within 0.6 km near the ground over the LP, forming positive feedback, and the collision–coalescence process is dominant.

Keywords: orographic cloud and precipitation; vertical structure; precipitation microphysical properties

1. Introduction

Orographic cloud and precipitation is an important factor affecting annual precipitation and river runoff in most areas of the world and is also the main source of precipitation in northwest China [1–3]. Terrain with different scales and morphological characteristics affects synoptic systems, resulting in dynamic and thermal effects, which have profound and complex impacts on the formation and development of clouds and precipitation [4–6]. The vertical structure and distribution of associated hydrometeors are fundamental aspects of cloud and precipitation research and relevant operations such as refined forecasting

and regional model improvement. The vertical structure of cloud and precipitation can be used to characterize the cloud and precipitation dynamics and macro- and micro-physical processes involved in hydrometeor growth and decay. These processes strongly affect precipitation efficiency and rainfall rate at the surface. Therefore, reliable detection of vertical structures and evolutions of clouds and precipitation moving over the terrain using remote sensing tools is critical for a better understanding of the inner microphysical processes and properties. In addition, abundant measurements can provide effective supporting data for research on artificial weather modification, cloud and precipitation mechanisms, and numerical forecasting [7–11].

Understanding the influence of topography on structures and microphysical characteristics of precipitating clouds plays an important role in the study of orographic clouds and precipitation. In the past 70 years, with the rapid development of meteorological detection technology, observational experiments of mountain meteorology have been carried out all over the world [12]. Kirshbaum et al. [13] studied the triggering effect of convective rain belts on small-scale terrain through observations and numerical simulations in Oregon, USA; results indicated that, in the front of orographic clouds, the orographic leeward waveforms updraft and trigger a leeward slope rain belt. Lee et al. [14] combined Doppler radar data and the numerical model to study the mechanism of precipitation enhancement near the Jeju Island Mountains during Typhoon Khanun. They suggested that precipitation on the windward slope is enhanced by the interaction of high-level falling particles (seeder) and low-level lifting particles (feeder). When the air enters a downslope area and suddenly meets the bottom of the terrain, the phenomenon of a “Water jump” occurs, which causes an increase of cloud and supercooled water between 3 and 6 km, and provides abundant liquid water for riming and condensation. Therefore, the seeder–feeder mechanism also significantly enhances the precipitation of the leeward slope. Houze et al. [3] found that ice crystal particles in stratiform precipitation formed over the terrain mainly grow through condensation and the collision-coalescence process in the case of stable stratification. However, when the stratification is weakly unstable, the airflow moving over the terrain will excite convective cells and produce abundant cloud water, which plays an important role in the precipitation process of both cold and warm clouds.

Recently, according to the present situation of drought and water shortage in the northwest of China, representative mountainous areas were selected to carry out the comprehensive detection and research of orographic clouds and precipitation, intending to understand further the structure of orographic clouds and characteristics of precipitation in northwest China [1,2,4,15–17]. Fu et al. [18] counted the cases of precipitation in the Himalayas from 1998 to 2012 and concluded from 7.5 km that ASL could be used as a boundary between shallow and deep precipitation due to the instability of the plateau atmosphere and strong surface heating, and weak convective precipitation is more likely to occur. Shao et al. [15] adopted an improved advanced regional predictional system (ARPS) model to simulate a summer topographic cloud and precipitation process in the Qilian Mountains and found that the steep topography on the northern slope is the main driving force of cloud and precipitation in the Qilian Mountains. Yu et al. [16] found that the topography of the Tian Mountains has little impact on the height distribution of snow and ice crystals in the upper layer but has a significant impact on their magnitudes and maintenance time. Cao et al. [17] compared and analyzed the cloud microphysical characteristics and bright bands of convective, stratiform, and shallow cumulus clouds and precipitation over ridges and valleys in the Liupan Mountains of China using observations from micro rain radar and microwave radiometer. Results showed that the topographic forcing made precipitating clouds’ physical and dynamic processes on mountain ridges more intense than those in valleys, and there were more hydrogels above the 0 °C isotherms in the precipitation process of stratiform clouds. He et al. [19] studied the vertical structure and difference between stratiform clouds and precipitation in south China and the Tibetan Plateau with ground-based remote sensing equipment and found that the melting layer in south China can be much higher and slightly thicker than those in the plateau area.

Additionally, several other studies (Zhong et al. [20]; Luo et al. [21]) found that, compared with plain areas, the precipitation intensity in the mountains can be relatively weaker, shallower, and more localized, and the vertical extension height of the mixed-phase layer is lower than plain areas. Meanwhile, mountain raindrops are generally smaller, and their distribution is more dispersed than in plain areas.

The Liupan Mountains are located in the southeastern part of northwest China, at the junction of Shaanxi, Gansu, and Ningxia provinces, with a ridge elevation of more than 2500 m. The eastern slope of the mountain is steep, while the western slope is gentle. As one of the few long and narrow mountains with a north-south orientation, the Liupan Mountains have been selected as a scientific test base by the Weather Modification Center (WMC) of the China Meteorological Administration (CMA) [22]. To study the impact of terrain on precipitation in northwest China, the WMC has built an observation system to detect the macro and micro characteristics of orographic clouds and precipitation in this mountainous area; the in-situ sites can be referred to in Figure 1. Based on the advantages of ground-based equipment, such as different wavelength radars, the objective of this paper is to explore the impact of the Liupan Mountains' topography on the vertical structures and microphysical characteristics of a mixed cloud and precipitation process that happened on 14 August 2020 in the northwest arid region. The remainder of the manuscript is organized as follows: Section 2 introduces the instruments used, measurements taken, and data processing methodologies; Section 3 details the results; Section 4 discusses the findings, which are further compared with other studies; Section 5 presents the conclusions.

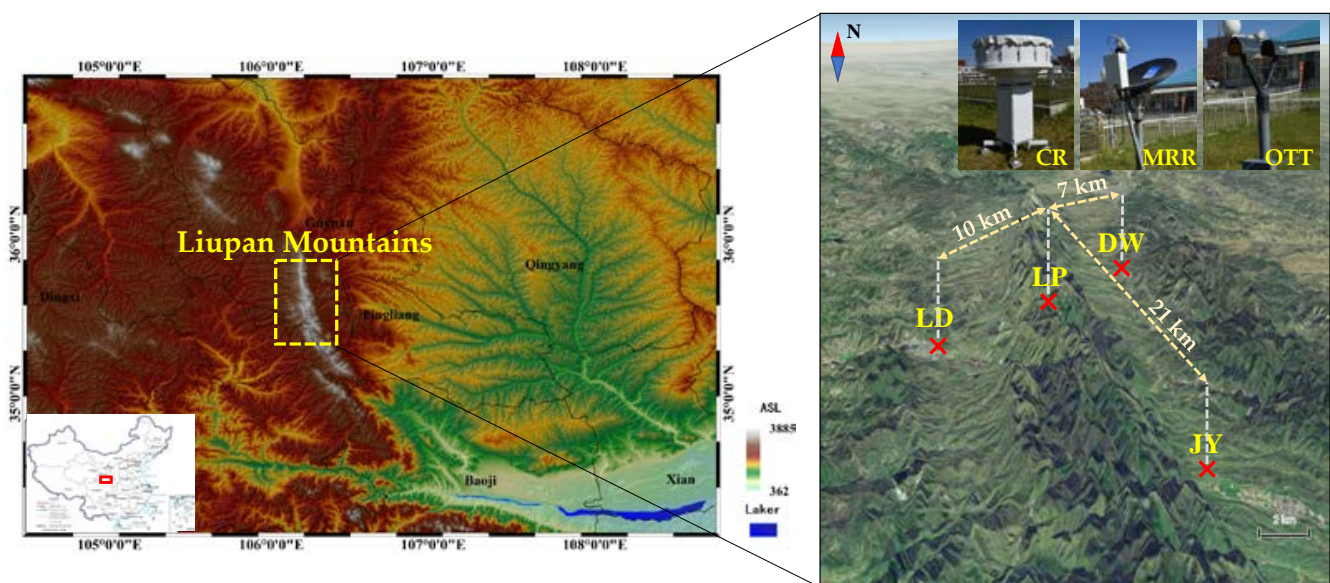


Figure 1. Geographical location and terrain of the Liupan Mountains, and the distribution of four observation sites, namely, the Longde (LD, 2079 m ASL, windward slope), Liupan (LP, 2842 m ASL, mountaintop), Dawan (DW, 1981 m ASL, leeward slope), and Jingyuan sites (JY, 1985 m ASL, leeward slope) and instrument scenes. The CR, MRR, and OTT denote Ka-band millimeter-wave cloud radar, K-band micro rain radar, and laser-based ground disdrometer, respectively.

2. Observation Sites, Instruments, and Measurements

2.1. Observation Sites

There are four observation sites located in the Liupan Mountains, and three of them are used in this study. As demonstrated in Figure 1, the Liupan site (LP, 106.12° E, 35.40° N), the main observation point in the Liupan Mountains, is located on the peak of the central area of the mountains, with an altitude of 2842 m, ASL. The Longde site (LD, 106.07° E, 35.37° N), about 10 km southwest of the LP, is situated in a typical representative area affected by the southwest airflow, which often prevails in the Liupan Mountains, and the

altitude is about 800 m lower than the LP. Statistical studies have shown that, during a total of 193 precipitation events in the Liupan Mountains over three years, 91.6% of the radar echoes moved from west to east, mainly in the summer [2]. Therefore, the site is largely considered to be the windward slope of the mountains. The Dawan site (DW, 106.16° E, 35.42° N) is located on the steep east slope (which is likely considered to be the leeward side) and is located about 7 km northeast of the LP site with an altitude of 1981 m, ASL.

2.2. Instruments and Measurements

At the observation sites, three types of ground-based remote sensors were employed for clouds and precipitation observation, including a K-band micro rain radar (MRR), a Ka-band millimeter-wave cloud radar (CR), and a laser-based ground disdrometer. Details of each instrument and its measurements are described as follows.

An MRR manufactured by METEK GmbH, Germany, has been widely used in the observation and study of microphysical and structural properties of precipitation [23–28]. The radar is a zenithal frequency-modulated continuous-wave radar with an operational wavelength of 12.38 mm (frequency: 24.23 GHz). The radar’s temporal and spatial resolutions are adjustable, which herein are set to 1 min and 150 m, respectively. The detectable radar range is from 150 to 4650 m; thus, the main measuring target of the radar is precipitating particles in the low to middle levels of the atmosphere. The MRR measurements include equivalent reflectivity factor Z_e (dBZ), raindrop spectrum $D \sim N(D)$ [D (mm) and $N(D)$ ($m^{-3} mm^{-1}$) are raindrop diameter and number concentration, respectively], and particle falling velocity V_t ($m s^{-1}$).

The CR is also a vertically pointing radar made by Xi’an Huateng Microwave Co., Ltd., China. The radar operates with a wavelength of 8.57 mm (frequency: 35 GHz) and can detect cloud and precipitation profiles within 0.12–20 km with a temporal resolution of 5 s and a spatial resolution of 30 m. Due to the shorter wavelength, shorter pulse width (0.2 μs), and narrower beam width (0.4°), the CR is much more sensitive to the non-precipitating cloud than the MRR and centimeter-wave weather radars and also has a higher resolution in space [29–32]. The CR measurements used herein are Z_e (dBZ), Doppler spectrum, and spectral width S_W ($m s^{-1}$). The main specifications of MRR and CR are summarized in Table 1.

Table 1. The main specifications of CR and MRR.

Parameters	CR	MRR
Transmitting frequency	35 GHz (Ka-band)	24.23 GHz (K-band)
Wavelength	8.57 mm	12.38 mm
Detection mode	Vertically pointing	Vertically pointing
Range resolution	30 m	150 m
Temporal resolution	5 s	10–3600 s (adjustable)
Nyquist velocity range	−13.92–13.92 $m s^{-1}$	−12.19–12.19 $m s^{-1}$
Detectable height range	0.12–20 km	0–4.65 km
Primary detection object	Non-precipitating clouds, weak precipitation	Precipitation
Measurements	Equivalent reflectivity factor (Z_e , dBZ), spectrum width (S_W , $m s^{-1}$), Doppler spectrum	Z_e (dBZ), particle falling velocity (V_t , $m s^{-1}$), raindrop spectrum

The used disdrometer is a second-generation Particle Size and Velocity disdrometer manufactured by OTT Hydromet, Germany, which has been commonly used in many scientific programs and research [24,33]. The OTT laser-based disdrometer (OTT) can simultaneously measure the raindrop diameter D (mm) and falling velocity V ($m s^{-1}$) according to the signal attenuation and duration when the raindrop passes the laser beam. The OTT has a sampling area of 54 cm^2 and a sampling interval of 1 min. Its raw data are reserved by dividing the diameter and falling velocity into 32×32 non-equidistant classes.

The measurable range of the D and V are from 0.062 to 24.5 mm and 0.05 to 20.8 m s⁻¹, respectively. For convenience, abbreviations of three instruments and physical quantities used in this paper can be found in Appendix A (Table A1).

Apart from the aforementioned instruments and measurements, three other types of data were also used to gain a better understanding of synoptic circumstances and evolutions of the analyzed cloud and precipitation processes. Specifically, the fifth-generation Earth Reanalysis Atmospheric data (ERA5, cds.climate.copernicus.eu) provided by European Center for Medium-Range Weather Forecasts (ECMWF) was used to analyze the weather background from a synoptic scale. The combined reflectivity, CR (dBZ), of the C-band weather radar at the Guyuan Station (a member of the Chinese Network Weather Radar and is located at the LP) was used to analyze the evolution principles and movement direction of the clouds and precipitation system, which further helped determine the precipitation types and windward slope. The C-band weather radar takes six minutes to perform a routine VCP-21 (Volume Coverage Pattern) scan that contains nine elevation layers (i.e., 0.5°, 1.5°, 2.4°, 3.4°, 4.3°, 6.0°, 9.9°, 14.6°, and 19.5°). It can provide observations with an effective detection radius of 150 km and a range gate spacing of 300 m. Finally, temperature measured by the ground thermometer screen, rain rate output from the ground tipping bucket gauges, and 10 m wind speed (all recorded at ground-based automatic weather stations) were also used. The average values of temperature recorded at the LD, LP, and DW were about 13.8, 8.4, and 12.9 °C, respectively, which proved that this is a liquid precipitation process. Meanwhile, the average wind speeds measured at 10 m height at the LD, LP, and DW were about 1.87, 2.37, and 1.61 m s⁻¹, respectively, demonstrating that wind speeds could not cause many biases in the rain rates' measurements.

2.3. Data Quality Control and Postprocessing

The electromagnetic wave of the Ka-band CR can be attenuated by the atmosphere and cloud precipitation during the propagation; therefore, an iterative procedure was used to correct the radar-measured Z_c in Appendix A, and afterwards considered that the CR-detected Doppler velocity included V_t (m s⁻¹) and vertical air velocity V_a (m s⁻¹), which are both important parameters of cloud dynamics. In this paper, the small particle tracing method proposed by Gossard et al. [34] and Kollias et al. [35] was used to derive V_a . The basic principles of the retrieval method can be briefly described: for the smallest particle that can be measured by high-sensitivity millimeter-wave radar, its falling speed is nearly negligible compared with the vertical air motions in convective clouds and precipitation. Thus, the smallest detectable particles can be regarded as moving with the wind, and their velocity bin of signal in the radar Doppler spectrum can be used to retrieve V_a . The diameter D_{trace} (mm) and falling velocity V_{trace} (m s⁻¹) of tracer particles are estimated by assuming the number concentration of them, and then V_a can be obtained by deducting V_{trace} from the Doppler velocity ω_0 [36] to reduce the error as much as possible, described as

$$V_a = \omega_0 - V_{trace} \quad (1)$$

Existing studies have found that the OTT can produce problematic data due to its inherent limitations or when under some special environment [37–39]. Therefore, the following technologies were implemented to improve the raw data accuracy.

First, considering the actual sensitivity of OTT and the size of the largest precipitating raindrop in the natural atmosphere, data in the first two diameter classes corresponding to the smallest particles and any data with $D > 6$ mm were both abandoned [40,41]. Second, if the D is smaller than the thickness of the laser beam, it will cause velocity measurement errors to some extent. In addition, strong wind shears or splashing effects of large raindrops hitting the surface of the instrument may lead to the V of certain values that are unrealistic during heavy rain. Accordingly, the theoretical calculation of V proposed by Atlas et al. [42] was used to reduce errors in the measured value. Moreover, the quality control process also includes eliminating $RSDs$ with a total raindrop number less than ten or $R < 0.01$ m s⁻¹,

which were treated as nonrainy samples [41]. After data quality control, the raindrop number concentration in each diameter class $N(D_i)$ ($\text{m}^{-3} \text{mm}^{-1}$) can be counted as follows,

$$N(D_i) = \frac{n(D_i)}{V(D_i) \times A \times \Delta t} \quad (2)$$

where D_i (mm) is the raindrop diameter for class i , $n(D_i)$ represents the raindrop number within class i , A (m^2 , 54 cm^2) denotes the sampling area, $V(D_i)$ (m s^{-1}) is the raindrop falling velocity for D_i , and Δt (60 s) is the sampling time. The mass-weighted mean diameter, D_m (mm), and generalized intercept parameter, N_w ($\text{m}^{-3} \text{mm}^{-1}$), can also be calculated as follows [43],

$$D_m = \frac{\sum_{i=1}^{32} D_i^4 \times N(D_i)}{\sum_{i=1}^{32} D_i^3 \times N(D_i)}, \quad (3)$$

$$N_w = \frac{128}{3D_m^4} \sum_{i=1}^{32} D_i^3 \times N(D_i) \quad (4)$$

3. Results

In the following subsections, the analyses, comparisons, and results regarding synoptic conditions, evolutions, vertical structures, and microphysical characteristics of mixed clouds and precipitation processes observed at different mountainous sites are presented in detail to explore the usage of multiple ground-based remote sensors in the orographic clouds and precipitation observation and to study the influence of terrains on clouds and precipitation processes and properties.

3.1. Synoptic Condition

Figure 2 shows the geopotential heights, horizontal winds, relative vorticities, and water vapor fluxes at 500 and 700 hPa before the occurrence of the mixed cloud and precipitation process in the Liupan Mountains on 14 August 2020. It can be seen that (Figure 2a) there was a shortwave trough at 500 hPa in the eastern Qinghai Province, and the mountains were affected by the warm and humid southwest airflow at the front of the trough. At 700 hPa (Figure 2b), a low-vortex circulation developed in the southwest of Gansu Province, and the south of the Ningxia Province was influenced by the south-southeast airflow in front of the vortex. The wind field exhibited a significant cyclonic shear, and the low airflow converged and raised, corresponding to the center of the positive value of relative vorticity (Figure 2d). There were strong water vapor belts both in the southwest and southeast of the Liupan Mountains, which transported large amounts of water vapor to the mountains (Figure 2c). Overall, the atmospheric conditions were favorable for the generation and development of clouds and precipitation in the upwind slope of the Liupan Mountains and its surrounding areas.

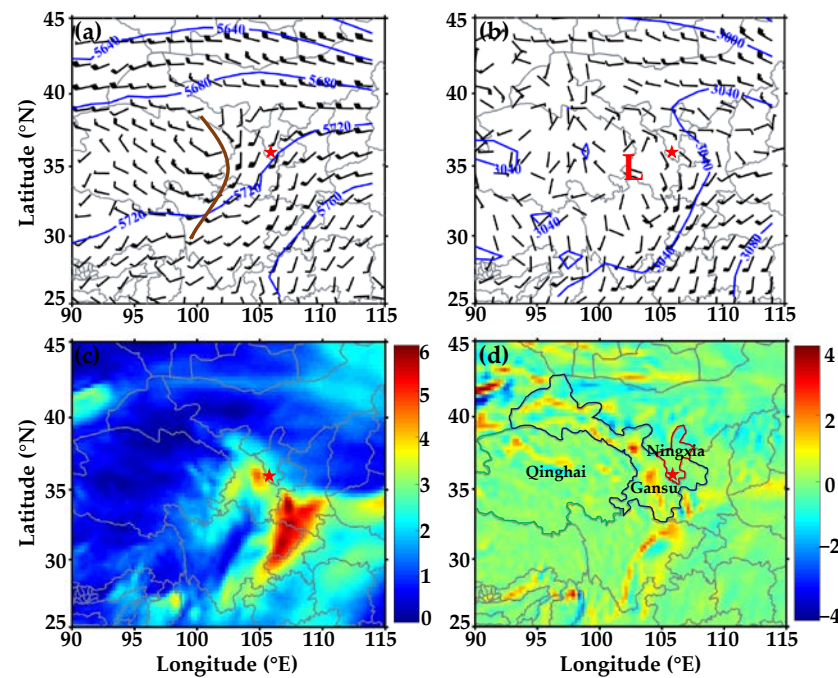


Figure 2. Weather charts at 0000 (UTC) on 14 August 2020 show (a) 500 hPa and (b) 700 hPa geopotential heights (blue line, unit: dagpm), horizontal winds (vector bar), and (c,d) represent integrated water vapor flux ($10^5 \text{ g} \cdot \text{m}^{-1} \cdot \text{s}^{-1}$) and 700 hPa relative vorticity (10^{-4} s^{-1}), respectively. The red pentagram denotes the location of the Liupan Mountains.

3.2. Evolution of the Cloud and Precipitation Process

The CR observed by the Guyuan C-band Doppler weather radar was further analyzed to briefly view the formation and evolution principles of the cloud and precipitation process on 14 August 2020. Figure 3 shows six moments of CRs of the cloud and precipitation from 0000 UTC to 1200 UTC on 14 August. Observations indicated that around 00 a.m. (0000 UTC, Figure 3a), the cloud and precipitation system were detected south of the Liupan Mountains, with echo intensities of 30–40 dBZ. Further, the system and its produced precipitation gradually covered the whole mountains. Near 0200 UTC (Figure 3b), the horizontal scale of clouds and precipitation had significantly increased, and echoes over the three in situ sites also greatly enhanced. Later, around ~0400 UTC (Figure 3c), the clouds and precipitation moved to the northeast and weakened to some extent. Around 0600 UTC (Figure 3d), the echo range covered by the system gradually reduced, and the radar echoes were almost concentrated over the mountains. Then, the system continuously moved to the northeast and finally moved out of the mountains. Meanwhile, it can be found that the system has changed from cumulus-mixed to shallow at ~0800 UTC (Figure 3e). Whereas, until ~1200 UTC (Figure 3f), a large sheet of echoes appeared again over the Liupan Mountains, but the clouds and precipitation seemed to become stratiform. The clouds and precipitation finally dissipated around 1500 UTC.

In summary, the clouds and precipitation over the Liupan Mountains were yielded by the weather system in the early stage before 0700 UTC, and their radar echoes were relatively strong. However, as the weather system moved away northeastward and dissipated, radar echoes significantly weakened. From 1000 UTC, sheet-like weak echoes triggered by the terrain appeared again over the mountains and lasted for about 3 h before dissipation. The general moving direction of this cloud and precipitation system was from the southwest to the northeast. Therefore, it can be determined that the LD site is on the upward slope, and the DW site is on the leeward slope.

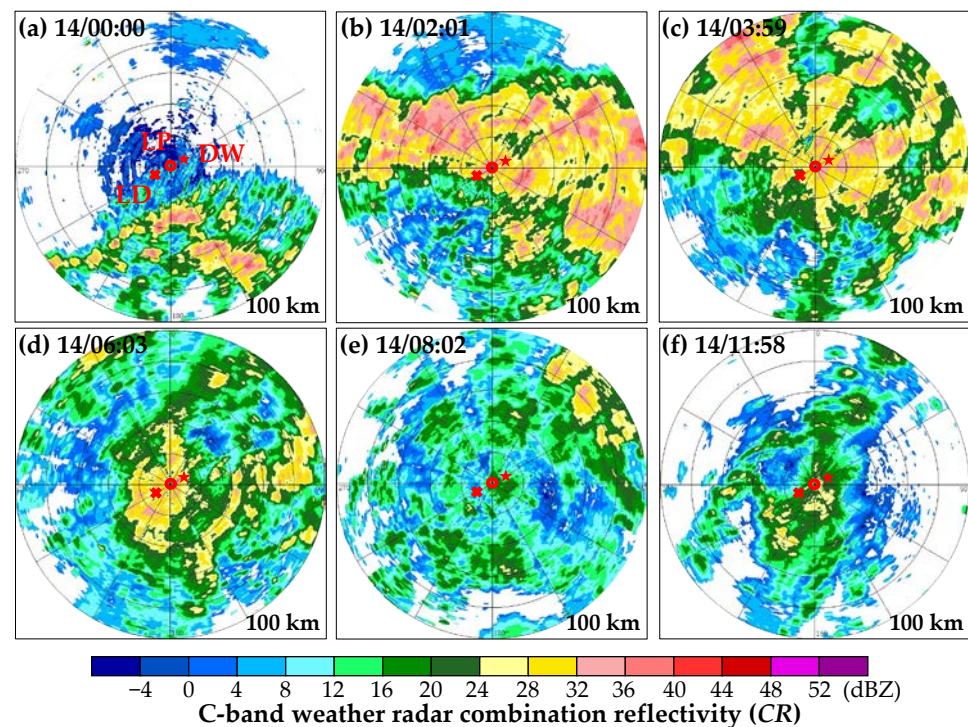


Figure 3. Combination reflectivity (CR, dBZ) images from the C-band Doppler weather radar at the Guyuan station for the mixed cloud and precipitation process on 14 August 2020; (a–f) represent six different moments, and the cross, circle, and asterisk denote the locations of the LD, LP, and DW sites, respectively.

In summary, the clouds and precipitation over the Liupan Mountains were yielded by the weather system in the early stage before 0700 UTC, and their radar echoes were relatively strong. However, as the weather system moved away northeastward and dissipated, radar echoes significantly weakened. From 1000 UTC, sheet-like weak echoes triggered by the terrain appeared again over the mountains and lasted for about 3 h before dissipation. The general moving direction of this cloud and precipitation system was from the southwest to the northeast. Therefore, it can be determined that the LD site is on the upward slope, and the DW site is on the leeward slope.

The Z_e and rain rate (R), severally detected by CR and OTT at three topographic sites of the Liupan Mountains, were analyzed and compared to view the aloft time-height cross-sections and surface rainfalls of the mixed clouds and precipitation process on 14 August 2020. As shown in Figure 4, comparing Z_e s among the LD, LP, and DW sites (Figure 4a–c), it can be seen that the echo distributions coincide well with similar appearances and vertical structures in both time and space under light-to-moderate rainfall circumstances on the ground, with R ranging from 0.1 to 7.5 mm h⁻¹ (Figure 4d). In comparison, Z_e and R at the LD remain the weakest and vigorously develop afterwards at LP after orographic uplifting. The results at DW are slightly stronger than LP. Regardless of the high-level cirrus, the flame-like cloud-top height (CTH) can develop to about 9 km. The 0 °C isotherm at about 5.4 km was detected by a ground-based microwave radiometer. Meanwhile, a remarkable bright band (BB) can be observed by the CR at a height from 5.4 to 5 km, which is ambiguous in CR images. The characteristics of the cloud-top with an up-rush trend, strong Z_e , and BB from 0000 to 0700 UTC indicate that this period is a cumulus mixed cloud precipitation stage. As the weather system weakened, the differences reflected in CTHs and R s among the three sites were obvious in the shallow precipitation stage from 0700 to 1000 UTC. Later, the Z_e s and R s indicated that the cloud and precipitation developed into stratiform with steady changes and clear BB. In summary, orographic uplifting makes

Z_e s and R s stronger at the LP site than the LD, and the close distance between LP and DW leads to the similarity of echoes and precipitation.

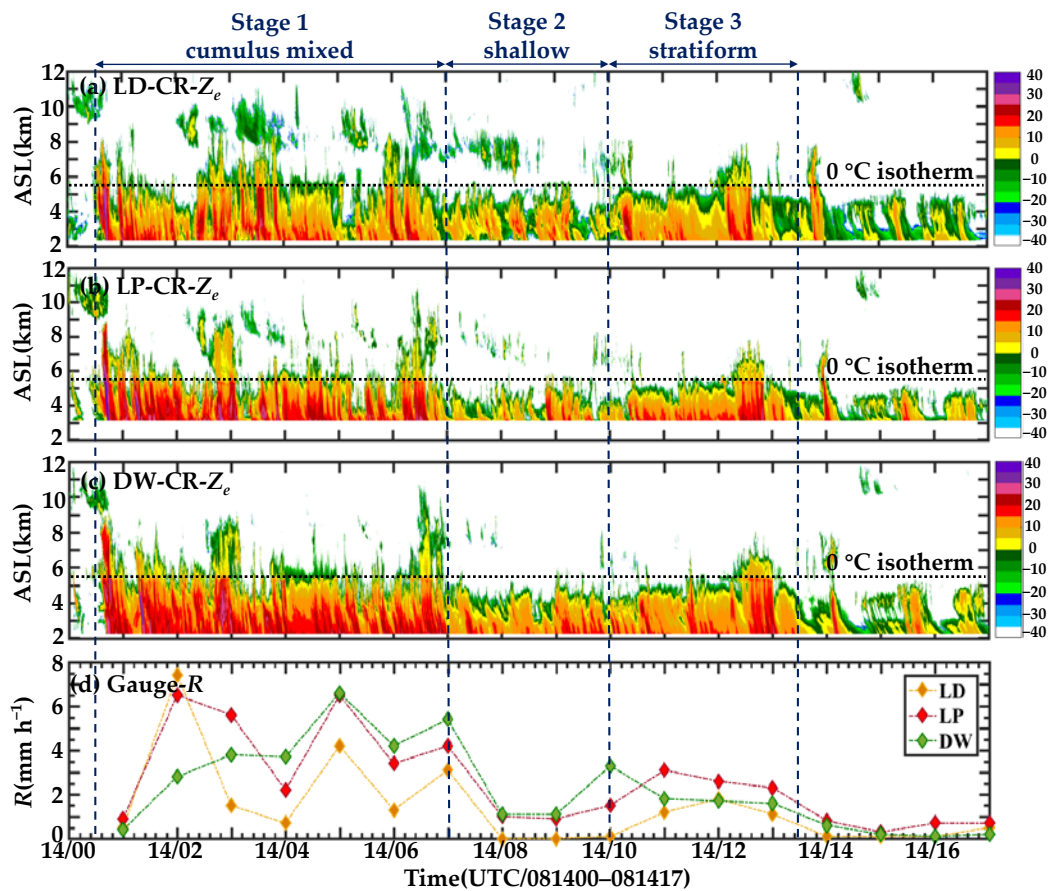


Figure 4. Time-height cross-sections of equivalent reflectivity factor (Z_e , dBZ), measured by the CR, and ground rain rate (R , mm h^{-1}), measured by the OTT, over three topographic sites for the mixed cloud and precipitation process on 14 August 2020; (a–c) represent Z_e s at the LD, LP, and DW sites, respectively. The black dotted line denotes the $0\text{ }^\circ\text{C}$ isotherm at about 5.4 km, ASL, and (d) represents ground hourly R s.

The horizontal and vertical structures of clouds and precipitation over three stations in the Liupan Mountains are affected by the changes in the weather system, and the ground R s presented corresponding changes; therefore, the process can be divided into different stages. According to classification schemes of cloud precipitation structures proposed by Bringi et al. (2003) [43] and Fabry et al. (1995) [44], the precipitation with $R > 0.5\text{ mm h}^{-1}$ and standard deviation of R (σ_v) $< 1.5\text{ mm h}^{-1}$ within at least 10 min was classified as stratiform precipitation; the precipitation with $R > 5\text{ mm h}^{-1}$ and $\sigma_v > 1.5\text{ mm h}^{-1}$ was determined as convective precipitation [45]; CTH lower than the height of $0\text{ }^\circ\text{C}$ isotherm with small R ($R < 4\text{ mm h}^{-1}$) was treated as shallow precipitation [44,46]. When both the BB structure and convection were observed on the radar echoes, the precipitation was further classified as cumulus mixed cloud precipitation [47]. Note that convection may break through the melt layer or exist beneath it.

According to the above-mentioned criteria, combined with the C-band Doppler weather radars' and CRs' detected results, the mixed cloud and precipitation process can be divided into four stages. This paper only discusses the first three stages due to small sample sizes in the last extinction stage; the first stage is cumulus mixed cloud and precipitation (0000–0700 UTC); the second stage is shallow clouds and precipitation (0700–1000 UTC); the third stage is stratiform clouds and precipitation (1000–1300 UTC).

3.3. Vertical Structures and Microphysical Properties of the Cloud Precipitation Process

To further compare the vertical developments and evolutions of the cloud precipitation process in different stages before and after being affected by topography, this subsection makes an in-depth analysis of the vertical structures and microphysical characteristics of three cloud and precipitation stages observed at LD, LP, and DW. First of all, normalized contoured frequency by altitude diagrams (NCFAD) for five physical quantities, namely $CR-Z_e$, $CR-V_a$, $CR-S_W$, $MRR-Z_e$, and $MRR-V_t$, are presented to show the vertical structural characteristics and differences. The NCFAD was initially used to display the statistical distribution characteristics of storms but only normalized the sum of the number of samples at its altitude level [48,49]. Later, the statistical method was improved, and samples at all altitude levels were normalized [50,51]. The method adopted in this study was used to calculate the percentage of frequencies with certain values in any certain altitude or range that accounts for the maximum frequency at all altitude levels, which has been widely used for model evaluations [52,53]. In addition to significant differences in vertical structures, different physical processes and microphysical properties of falling raindrops over three topographic sites were also inferred and compared using the NCFADs of MRR-measured D_m , N_w , and averaged raindrop spectra below the 0 °C isotherm.

3.3.1. Cumulus Mixed Cloud Precipitation Stage

To ascertain discrepancies in radar variables at different topographic sites, Figure 5 gives the NCFADs and median profiles of $CR-Z_e$, $CR-V_a$, $CR-S_W$, $MRR-Z_e$, and $MRR-V_t$ for the cumulus mixed cloud precipitation stage over LD, LP, and DW. The vertical distributions of these radar quantities reflect comprehensive results of macro and micro characteristics, such as the development and retention of particles in clouds and precipitation [54]. During the whole process, this stage possesses the maximum R , strongest echo, and highest CTH among the three stages, and the heaviest precipitation occurs at the LP site. Meanwhile, the flame-like CTH develops to about 9 km, indicating the existence of abundant water vapor that invigorates the fast growth of hydrometeors at this stage.

In terms of NCFADs and median profiles, Z_{es} over the LD site are the weakest, and variation trends and magnitudes of Z_{es} over DW are more similar to those over LP. Considering stronger attenuations of $CR-Z_{es}$ caused by the longest path for particles falling, Z_{es} over DW should be slightly stronger than that over LP (Figure 5(b4)). Even if maximum cumulative precipitation was observed at LP, Z_{es} over DW are still maintained due to the depletion and production of cloud and rain particles that nearly keep the balance. From the vertical distribution, the clouds over the LD site are still in development from 9 to 5.4 km with Z_{es} of ice particles ranging between -10 and 0 dBZ and present a weak updraft that is detectable in the clouds. As the cloud and precipitation move east, the dynamical and microphysical processes affected by orographic uplifting and the cloud's inner development mechanisms become more active and efficient [17]. Figure 5(e2) shows that the vertical distribution ranges of V_{as} are wider over LP; particularly, heavier rainfalls cause downdrafts that are significantly larger than those over LD. Meanwhile, Z_{es} over LP increases faster, caused by particles vigorously growing, as promoted by the updrafts. In the melting layer, Z_{es} , V_{ts} , and S_{WS} sharply increase, owing to the hydrometeor phase change. Z_{es} and S_{WS} of falling raindrops steadily increase again from the bottom of BB to the ground, and Z_{es} over the DW site that reach the ground have the largest performance, as caused by the longest falling path for particles, followed by the mountaintop [4,54–56]. The V_{ts} driving surrounding air downward remain at the maximum; meanwhile, downdrafts dragging raindrops down dominate within all altitudes of the cloud precipitation over DW. Therefore, a positive feedback mechanism can be concluded between falling raindrops and downdrafts, which can also be proved over LP, where both values of downward V_{as} and V_{ts} significantly increase from 4 km to the ground.

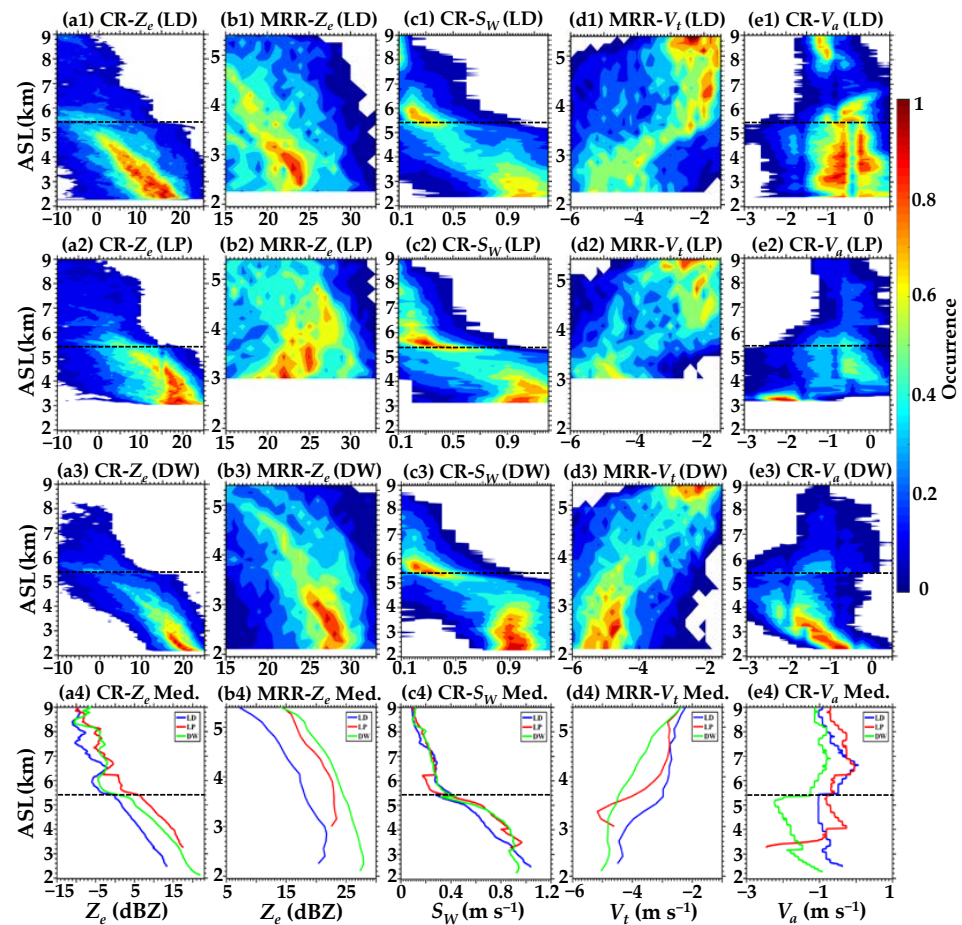


Figure 5. Normalized contoured frequency by altitude diagrams (NCFADs) of equivalent reflectivity factor (Z_e , dBZ), spectrum width (S_W , $m s^{-1}$), and vertical air velocity (V_a , $m s^{-1}$) measured by the CR, and Z_e (dBZ) and particle falling velocity (V_t , $m s^{-1}$) measured by the MRR for cumulus mixed cloud and precipitation stage. Subfigures (a1–e1), (a2–e2), and (a3–e3) represent the results at the LD, LP, and DW sites, respectively; (a4–e4) denote median profiles (Med.) of radar variables; the black dotted line represents the $0\text{ }^{\circ}\text{C}$ isotherm at about 5.4 km, ASL.

The falling raindrops can undergo evaporation, fragmentation, and collision-coalescence processes below $0\text{ }^{\circ}\text{C}$ isotherm and exhibit different microphysical properties over different topographic positions. Hence, NCFADs and median profiles of MRR-measured D_m , $\log_{10}N_w$, averaged $RSDs$, and OTT-measured-ground $RSDs$ under $0\text{ }^{\circ}\text{C}$ isotherm for the cumulus mixed clouds and precipitation stage are further compared, as shown in Figure 6. Results show that D_m s and N_w s of high-frequency distributions are both concentrated in small values [40,57,58].

The D_m s (N_w s) over LD steadily increase (decrease) as heights decrease and are the smallest, corresponding to the weakest Z_e s and R_s among the three sites. The wider ranges of vertical distributions of D_m s and N_w s over LP indicate that the cloud’s inner microphysical processes become more drastic in contrast to LD and DW after an orographic uplift [17,59].

The median profiles of N_w s (Figure 6(b4)) reveal that the maximum N_w during 4–5.4 km over the LP site corresponds to much higher number concentrations of N ($m^{-3} mm^{-1}$) of small raindrops, which can reach 10^5 magnitudes (Figure 6(c2)) than those at the other two sites. This finding is consistent with the conclusions of Sumesh et al. [60] and He et al. [19] that small particles possess significant N_s at high-altitude regions.

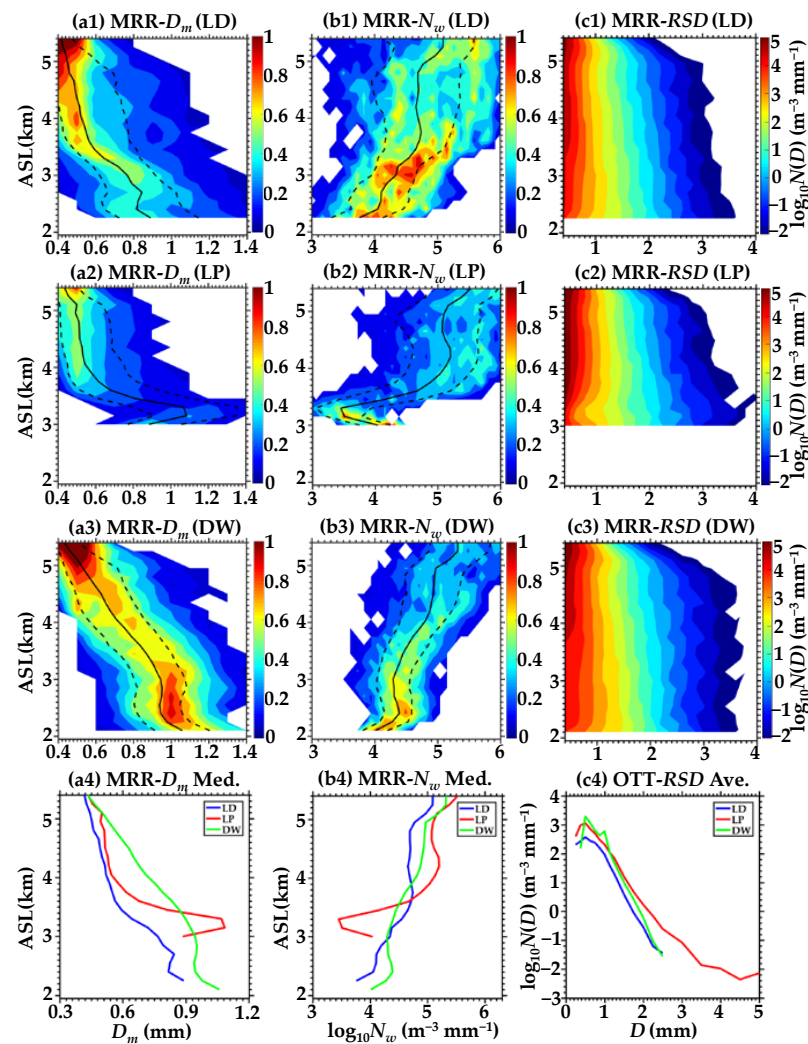


Figure 6. NCFADs of the mass-weighted mean diameter D_m (mm) and the logarithm of the generalized intercept parameter $\log_{10}N_w$ ($\text{m}^{-3} \text{mm}^{-1}$) for the cumulus mixed cloud and precipitation stage over the (a1,b1) LD, (a2,b2) LP, and (a3,b3) DW sites. Contours represent occurrence. The black dashed lines represent the 25th, 50th, and 75th percentiles. Subfigures (a4,b4) are the median profiles of D_m and $\log_{10}N_w$ over three sites. Vertical distribution of raindrop size distribution RSDs for the cumulus mixed cloud and precipitation stage over (c1) LD, (c2) LP, and (c3) DW. Contours represent $\log_{10}N(D)$ ($\text{m}^{-3} \text{mm}^{-1}$), and (c4) is averaged RSDs on the ground at LD, LP, and DW.

From 4.0 to 3.3 km over LP, N_s of small raindrops ($D < 1$ mm) suddenly decrease, while N_s of large raindrops ($D > 2$ mm) increase, indicating the collision-coalescence process dominates [23,61,62]. From 3.3 km to the ground, the increasing N_s of small raindrops and the decreasing N_s of medium-to-large raindrops denote that the fragmentation processes dominate near the ground, which is consistent with the D_m s (N_w s) decrease (increase) (Figure 6(a,b2)). Compared with the LD and LP sites, increments of D_m s over DW perform faster from 0 °C isotherms, owing to the maximum downward V_{as} and V_{ts} . At 2.8–2.4 km, D_m s (N_w s) slightly decrease (increase) corresponding to the increasing N_s of small raindrops and decreasing N_s of medium-to-large raindrops (Figure 6(c3)), suggesting that the fragmentation process dominates, which is consistent with the maximum N_s of small raindrops on the ground (Figure 6(c4)).

In summary, the changes of RSD versus heights over LD are inapparent, and the evaporation process dominates, while the evaporation, fragmentation, and collision-coalescence processes are all important over LP, which is similar to results of convective cloud and

precipitation at higher elevations of Li et al. [6], and the fragmentation process is dominant over DW.

3.3.2. Shallow Cloud Precipitation Stage

The NCFADs and median profiles of CR- Z_e , CR- V_a , CR- S_W , MRR- Z_e , and MRR- V_t for the shallow cloud and precipitation stage over LD, LP, and DW are depicted in Figure 7. The CTHs below 0 °C isotherms are relatively low at this period, with the minimum R and weakest echo during the whole process. It is drizzling at the LD site; nevertheless, Rs at LP and DW are slightly heavier, ranging from 2 to 4 mm h⁻¹, and the heaviest precipitation occurs at DW.

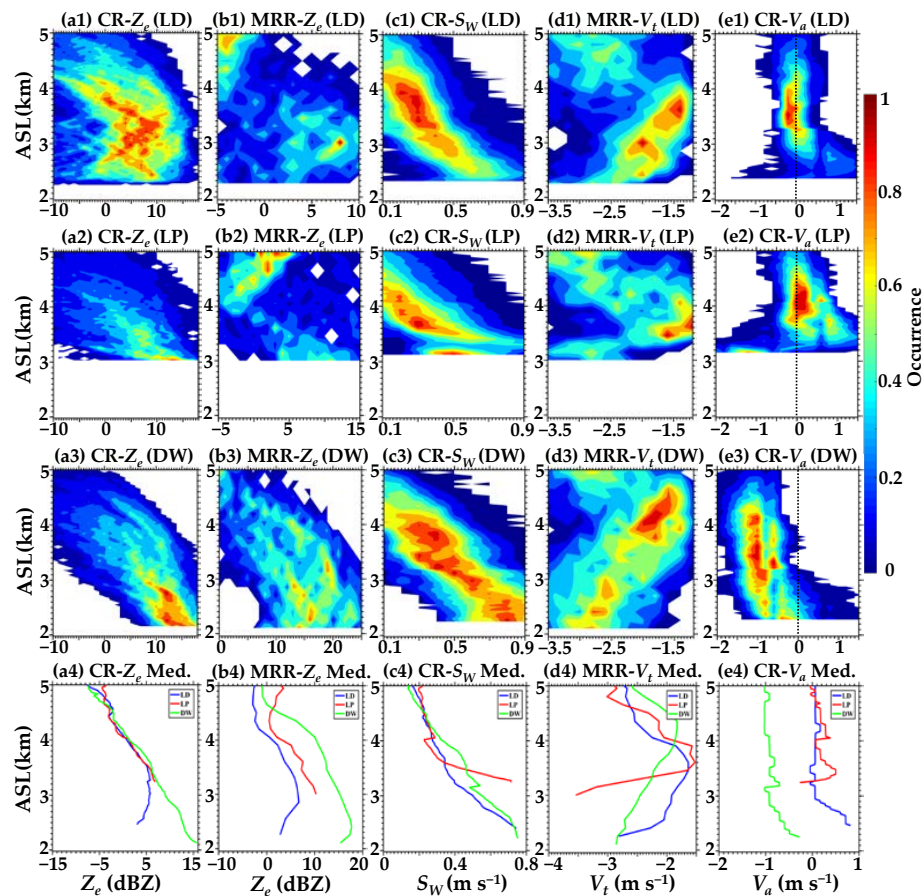


Figure 7. Normalized contoured frequency by altitude diagrams (NCFADs) of equivalent reflectivity factor (Z_e , dBZ), spectrum width (S_W , m s⁻¹), and vertical air velocity (V_a , m s⁻¹) are measured by the CR, and Z_e (dBZ) and particle falling velocity (V_t , m s⁻¹) are measured by MRR for the shallow cloud and precipitation stage. Subfigures (a1–e1), (a2–e2) and (a3–e3) represent the results at the LD, LP, and DW sites, respectively, and (a4–e4) denote median profiles (Med.) of radar variables. The black dotted line represents the 0 m s⁻¹ isoline.

Compared with the convective or stratiform stages, the Z_e s of the shallow cloud and precipitation stage always remained the weakest [23]. In this stage, differences between CTHs and Z_e s over the three sites are more pronounced. From the perspective of vertical distributions, CTHs over the LD are slightly higher than those over the LP (Figure 4a,b), and corresponding Z_e s (Figure 7(a1,a4,b1,b4)) reach the peak as raindrops fall to about 3.5 km, and then gradually weaken from 3.5 km to the ground, concentrated in 0–10 dBZ. Meanwhile, the S_W s, V_t s, and downward V_a s over LD (Figure 7(b1–e1,b4–e4)) all perform the minimum corresponding to the weakest R on the ground. However, the Z_e s over LP and DW (Figure 7(a4–b4)) both maintain steady growth from CTHs to the ground, and the Z_e s over DW are slightly larger in accordance with the strongest R. The vertical distribution

ranges of V_{as} (Figure 7(e2,e4)) over the LP site are wider than the other sites, and most of them are concentrated in the updrafts owing to orographic uplifting. Meanwhile, downdrafts near the ground become stronger than those over LD, attributing to heavier precipitation. The DW site is dominated by downdrafts, of which the result is the same as found in the previous stage; however, smaller values in this stage were caused by weaker precipitation. According to the comparisons of V_{ts} (Figure 7(d4)), the initial free-fall height of raindrops over LD and LP is consistent at about 3.6 km, while the counterpart over DW is about 4.4 km, which may be caused by the maximum downdraft over DW and positive feedback mechanism mentioned in the last subsection.

Figure 8 provides the NCFADs and median profiles of MRR-measured D_m , $\log_{10}N_w$, and averaged $RSDs$ under $CTHs$ and OTT-measured ground $RSDs$ for the shallow cloud and precipitation stage at the LD, LP, and DW sites, respectively. With the decrement of R_s and Z_{es} compared with the previous stage, the N_s of raindrops with different D_s also decrease at the same site [63].

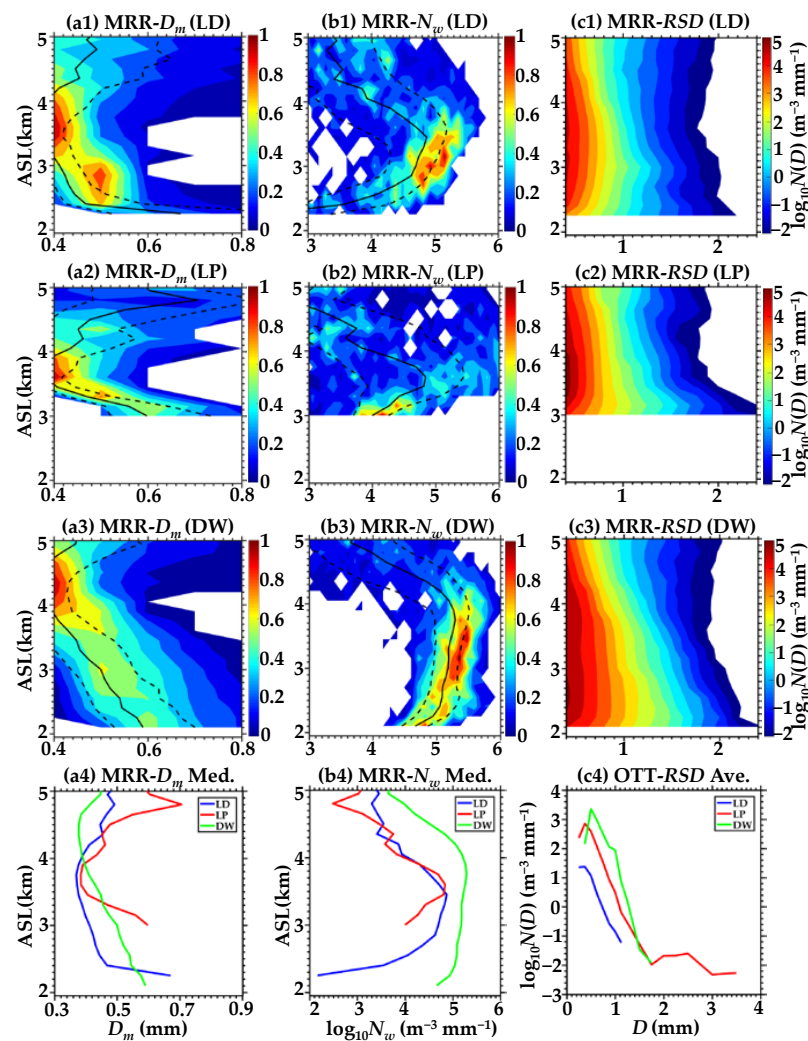


Figure 8. NCFADs of the mass-weighted mean diameter D_m (mm) and the logarithm of the generalized intercept parameter $\log_{10}N_w$ ($m^{-3} mm^{-1}$) for the shallow cloud and precipitation stage over (a1,b1) the LD, (a2,b2) LP, and (a3,b3) DW sites. Contours represent occurrence. The black dashed lines represent the 25th, 50th, and 75th percentiles, and (a4,b4) are median profiles of D_m and $\log_{10}N_w$ over three sites. Vertical distribution of raindrop size distribution $RSDs$ for the shallow cloud and precipitation stage over (c1) LD, (c2) LP, and (c3) DW. Contours represent $\log_{10}N(D)$ ($m^{-3} mm^{-1}$), and (c4) is averaged $RSDs$ on the ground at LD, LP, and DW.

For the cloud and precipitation in this stage, warm processes with liquid hydrometeors dominate. The measured $RSDs$ usually possess a relatively small-sized maximum D and high N_s of small raindrops near the ground [23], which is consistent with the results in Figure 8(c4). N_s of raindrops with different D_s over three sites from $CTHs$ to 3.5 km are continuously increasing owing to the low $CTHs$, especially for N_s of small raindrops, wherein their maximum can reach $10^5 \text{ m}^{-3} \text{ mm}^{-1}$ over the LP and DW sites, while N_{ws} over the DW are largest among three sites at all altitudes. N_s of small-to-medium raindrops and N_{ws} decrease by the fastest rate over the LD site from 3 km to the ground, corresponding to the weakening Z_{es} (Figure 7(a1)) and the smallest N_s of small raindrops on the ground (Figure 8(c4)). Considering the relatively long falling path over LD and much lower relative humidity ($RH\% \sim 86$) in the low levels than those of the LP and DW sites, the evaporation process at LD can be much stronger with the relevant weakest R_s and Z_{es} [6,64,65]. From 3.5 to 3.2 km (Figure 8(c2)), the sudden decrease of N_s for small raindrops and sharp increase of N_s for medium-to-large raindrops suggest that the collision-coalescence process dominates over the LP site, resulting in decreasing (increasing) N_{ws} (D_{ms}) and larger raindrops on the ground than those observed at LD and DW.

3.3.3. Stratiform Cloud and Precipitation Stage

The NCFADs and median profiles of $CR-Z_e$, $CR-V_a$, $CR-S_W$, $MRR-Z_e$, and $MRR-V_t$ for the stratiform cloud precipitation stage, the most stable process of cloud and precipitation with time, over the LD, LP, and DW sites are illustrated in Figure 9. The $CTHs$ in this stage develop to about 6 km, and the heights of 0°C isotherms are measured at about 5.4 km. R_s detected on the surface of the three sites are all between $1\text{--}3 \text{ mm h}^{-1}$, with the heaviest rain on LP and the abidingly weakest on LD.

The NCFADs imply a narrower frequency distribution, the vertical distributions of each radar quantity among the three sites are semblable with more apparent bright band structures than those of the first stage (Figure 9). The weakest Z_{es} over LD and the strongest Z_{es} over LP perfectly match the intensity of R_s on the ground (Figures 4d and 9(a1,a2)). From the perspective of vertical distributions, Z_{es} from the $CTHs$ to 0°C isotherms over the LP site (Figure 9(a4)) perform significantly stronger than those over the LD and DW sites, indicating that there are more hydrometeors or the formation and growth rates of ice particles are faster [6,17,23]. The abrupt changes of Z_{es} , S_{WS} , V_{ts} , and V_{as} (Figure 9(a4–e4)) can be found as height decreases from 5.4 to 5.0 km, particularly a significant increase in Z_{es} and S_{WS} over DW. Moreover, maximum V_t is observed at the bottom of the melting layers [23]. Within 0.6 km above the surface of the LP (Figure 9(c4,d4)), S_{ws} and V_{ts} of raindrops rapidly increase, which phenomenon occurs in all three stages, manifesting that orographic forcing makes the microphysical and dynamic processes of cloud precipitation on the mountaintop more active and intense. Compared with the V_{as} over the three sites (Figure 9(e1–e4)), the updrafts over LP are more prominent than those over LD; meanwhile, DW is persistently dominated by downdrafts, suggesting again that topography has influences on the dynamic structure of cloud precipitation.

The NCFADs imply a narrower frequency distribution, the vertical distributions of each radar quantity among the three sites are semblable with more apparent bright band structures than those of the first stage (Figure 9). The weakest Z_{es} over LD and the strongest Z_{es} over LP perfectly match the intensity of R_s on the ground (Figures 4d and 9(a1,a2)). From the perspective of vertical distributions, Z_{es} from the $CTHs$ to 0°C isotherms over the LP site (Figure 9(a4)) perform significantly stronger than those over the LD and DW sites, indicating that there are more hydrometeors or the formation and growth rates of ice particles are faster [6,17,23]. The abrupt changes of Z_{es} , S_{WS} , V_{ts} , and V_{as} (Figure 9(a4–e4)) can be found as height decreases from 5.4 to 5.0 km, particularly a significant increase in Z_{es} and S_{WS} over DW. Moreover, maximum V_t is observed at the bottom of the melting layers [23]. Within 0.6 km above the surface of the LP (Figure 9(c4,d4)), S_{ws} and V_{ts} of raindrops rapidly increase, which phenomenon occurs in all three stages, manifesting that orographic forcing makes the microphysical and dynamic processes of cloud precipitation

on the mountaintop more active and intense. Compared with the V_{as} over the three sites (Figure 9(e1–e4)), the updrafts over LP are more prominent than those over LD; meanwhile, DW is persistently dominated by downdrafts, suggesting again that topography has influences on the dynamic structure of cloud precipitation.

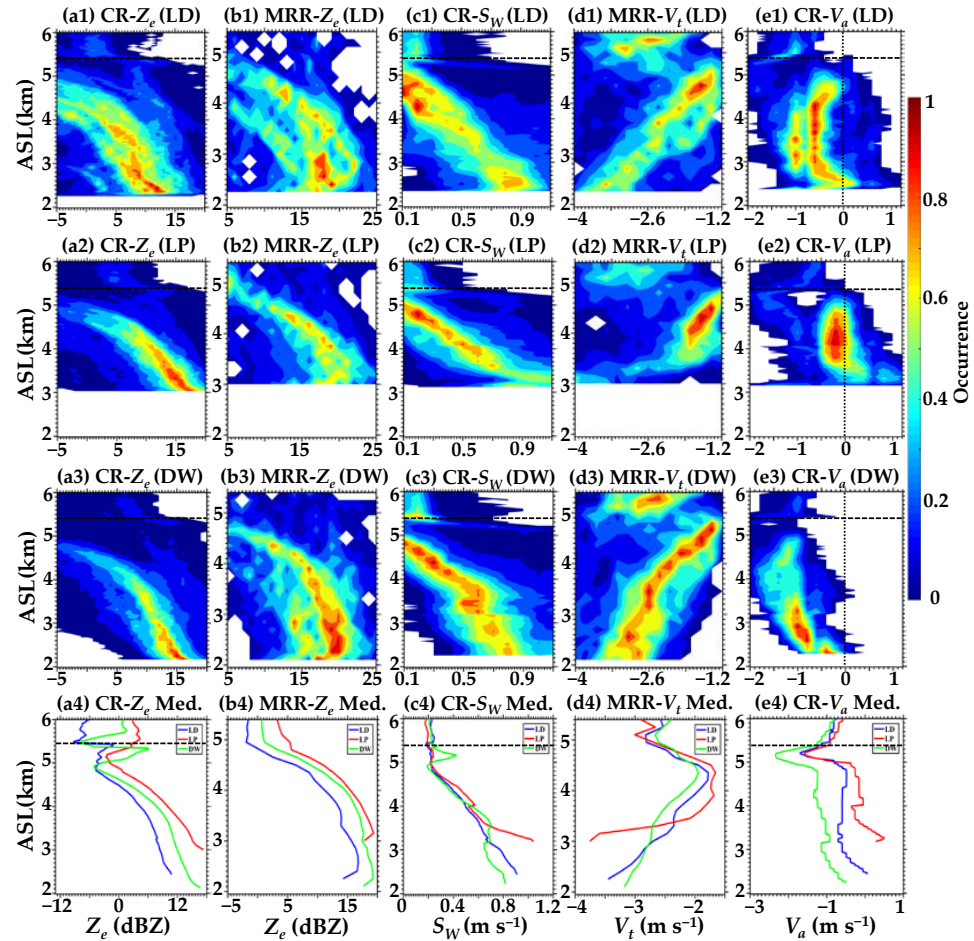


Figure 9. Normalized contoured frequency by altitude diagrams (NCFADs) of equivalent reflectivity factor (Z_e , dBZ), spectrum width (S_W , $m s^{-1}$) and vertical air velocity (V_a , $m s^{-1}$) measured by the CR, and Z_e (dBZ) and particle falling velocity (V_t , $m s^{-1}$) measured by the MRR for the stratiform cloud and precipitation stage. Subfigures (a1–e1), (a2–e2) and (a3–e3) represent the results at the LD, LP, and DW sites, respectively, and (a4–e4) denote median profiles (Med.) of radar variables. The black dotted line represents the $0\text{ }^{\circ}\text{C}$ isotherm (horizontal) at about 5.4 km, ASL, and $0\text{ }m s^{-1}$ isoline (vertical).

Figure 10 shows NCFADs and median profiles of MRR-measured D_m , $\log_{10}N_w$, and averaged $RSDs$ and OTT-measured ground $RSDs$ under $0\text{ }^{\circ}\text{C}$ isotherms for the stratiform-precipitation stage over the LD, LP, and DW sites. N_w s in this stage are the largest compared with the first two stages; moreover, the vertical distribution ranges of D_m s over the three sites are fairly consistent.

The variation trends of vertical distributions of D_m s and N_w s over the LD site are similar to the DW (Figure 10(a1,a3,b1,b3)), with the decrements and increments alternately changing from $0\text{ }^{\circ}\text{C}$ isotherms to the ground, but the values over LD are smaller, coinciding with the minimum Z_e s. Nevertheless, the most significant change is observed over the LP site (Figure 10(b2,b4)) with the largest magnitude of N_w s at most altitudes, demonstrating that the process of raindrops falling is much more complicated [57,66].

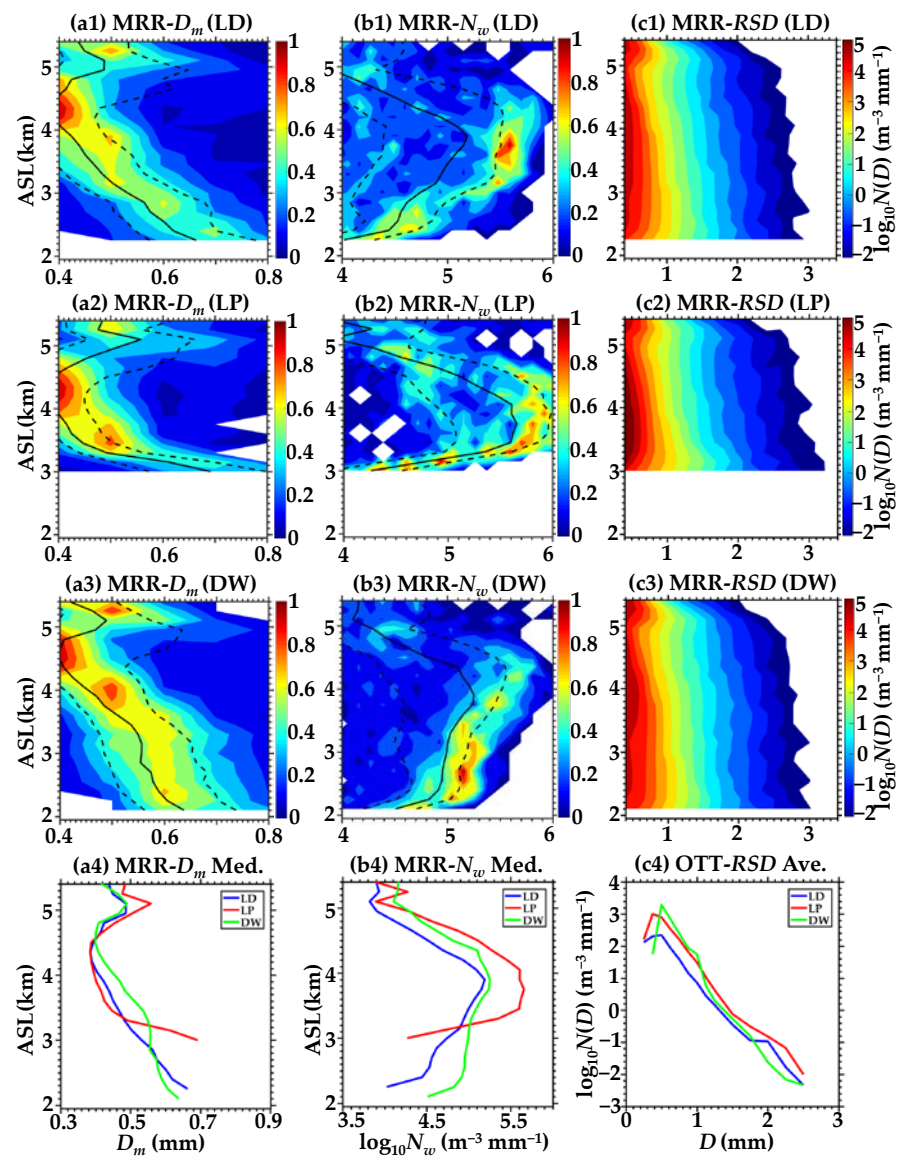


Figure 10. NCFADs of the mass-weighted mean diameter D_m (mm) and the logarithm of the generalized intercept parameter $\log_{10}N_w$ ($m^{-3} mm^{-1}$) for the stratiform cloud and precipitation stage over (a1,b1) LD, (a2,b2) LP, and (a3,b3) DW. Contours represent occurrence. The black dashed lines represent the 25th, 50th, and 75th percentiles. Subfigures (a4,b4) are median profiles of D_m and $\log_{10}N_w$ over the three sites. Vertical distribution of raindrop size distribution RSDs for the stratiform cloud and precipitation stage over (c1) LD, (c2) LP, and (c3) DW. Contours represent $\log_{10}N(D)$ ($m^{-3} mm^{-1}$). (c4) is averaged RSDs on the ground at the LD, LP, and DW.

The ranges of D_m 's distributions are the widest in melting layers from 5.4 to 5.0 km, and then become narrow as the falling raindrops are affected by the evaporation, fragmentation, and collision-coalescence processes [6,55,67]. The highest N_s of small raindrops reached $10^5 m^{-3} mm^{-1}$ over the LP site (Figure 10(c2)), which this observation is much higher than those over south China and the Tibetan Plateau [19]. Given that larger ice particles fall on the windward slope while smaller ones are transported farther to the peak and leeward slope by advection [3,59]. Over the LP site, N_w s (Figure 10(b2)) rapidly decreases again from 3.6 km to the ground, in agreement with the decreasing (increasing) N_s of small (large) raindrops (Figure 10(c2)) and manifesting that the collision-coalescence process dominates near the ground, the same results as found in the previous two stages. When raindrops reach the surface, the highest N_s of small raindrops and N_w s at the DW site (Figure 10(b4,c4)) may be caused by the fragmentation process.

4. Discussion

In this section, the characteristics of *RSDs* in the Liupan Mountains at three stages are compared with those obtained in other regions in China.

In contrast to the features of *RSDs* of convective cloud and precipitation during the Asian summer monsoon season or summer in eastern China [23,28], the averaged D_m - $\log_{10}N_w$ pairs, which are roughly inferred to be maritime as reported by Bringi et al. [43], the results of the cumulus mixed cloud precipitation in the Liupan Mountains possess comparable properties with small D_{ms} and high N_{ws} . However, the values of D_{ms} (0.4–1 mm) and N_{ws} (3.4 – $5.5 \text{ m}^{-3} \text{ mm}^{-1}$) are slightly smaller than those for convective clouds and precipitation, as aforementioned, which may be due to the weak convection and precipitation in this study. Moreover, the characteristics of *RSDs* in this study exhibit smaller D_{ms} and larger N_{ws} compared with those from convective clouds and precipitation observed during the Meiyu season in eastern China [45] or summer in the central Tibetan Plateau, regardless of the continental convection during the daytime or maritime convection at night [41]. The above discrepancies and signatures of *RSDs* may be caused by the high N_s of small raindrops in the Liupan Mountains.

The shallow clouds and precipitation have received little attention in continental regions, generally with the smallest (highest) D_{ms} (N_{ws}) in comparison with the convective and stratiform clouds and precipitation [28]. It can be found that the vertical structure of radar variables and characteristics of *RSDs* over the three sites in the Liupan Mountains significantly differed due to the strong localization of the shallow cloud and precipitation. The D_{ms}' values (0.38–0.7 mm) observed in this study are comparable to those of the shallow rain in eastern China during the Asian monsoon season or summer [23,28]; however, N_{ws} at the LD and LP sites (2.2 – $4.8 \text{ m}^{-3} \text{ mm}^{-1}$) are slightly lower, and the interval range of N_{ws}' values over the DW site (3.6 – $5.3 \text{ m}^{-3} \text{ mm}^{-1}$) is the closest to aforementioned research.

There are no significant changes in N_s of raindrops, particularly small raindrops, over the LD and DW sites below melting layers, and this is consistent with the conclusions of stratiform clouds and precipitation in eastern China [24]. Compared with findings of stratiform rain in eastern China during the Meiyu season or the summer and in the central Tibetan Plateau, the D_{ms} (0.3–0.7 mm) are smaller, and N_{ws} (3.8 – $5.7 \text{ m}^{-3} \text{ mm}^{-1}$) are much higher in this study [28,41,45,68]. Considering that smaller particles can be transported further to the mountaintop and leeward slope by advection [3,59], there are fewer evaporation processes of small raindrops due to the relatively short path of falling raindrops.

In addition, it is worth noting that the results of decreasing (increasing) N_{ws} (D_{ms}) near the ground and larger raindrops on the ground at the LP site than those observed at LD and DW are caused by orographic forcing, which can make the microphysical and dynamic processes of cloud and precipitation over the LP site more active and intense [17,59]; hence, the vertical distribution of *RSDs* obviously changes versus heights with the collision-coalescence process dominating at corresponding altitudes near the ground. According to Low and List [62], raindrops ($D < 0.6 \text{ mm}$) will only coalesce with larger raindrops if colliding, which might demonstrate that the coalescence processes (accompanied by abundant small raindrops) are more probable over the LP site when the collision processes occur.

The results are not necessarily conclusive due to the limited samples of cloud and precipitation episodes. Meanwhile, the variations of *RSDs'* characteristics among the above-mentioned studies are probably related to the different data samples, geographical locations, and instruments used [28]. Therefore, more datasets can be further used to analyze the microphysical processes of orographic clouds and precipitation, not just one cloud and precipitation event, and more detailed studies are needed to understand the vertical structures and microphysical characteristics better.

5. Conclusions

Based on the measurements of CR, MRR, OTT, and other ground-based equipment, vertical structures and microphysical characteristics of a mixed cloud and precipitation process, successively passes through the LD, LP, and DW sites were comprehensively

investigated and compared to explore the influences of the Liupan Mountains' topography on cloud and precipitation in northwest China. The main conclusions can be summarized as follows.

The properties of the mixed cloud precipitation process markedly differ with time; therefore, it can be divided into three stages, namely, the cumulus mixed cloud precipitation, shallow cloud precipitation, and stratiform cloud precipitation stages. It can be found that the vertical structure and macro- and micro-physical characteristics over the three sites are relatively similar in the third stage than those in the first stage, of which the mountain can slightly raise $CTHs$ over the LP and might lead to enhanced riming of supercooled liquid water in the third stage. However, the differences over the three sites (mainly reflected in $CTHs$ and Rs) are significant in the shallow cloud precipitation stage due to the strong localization. Moreover, it can also be found that during the whole cloud and precipitation process, topographic uplifting makes Rs stronger at the LP site.

The updrafts and downdrafts exist simultaneously over the LD site as the cloud and precipitation system is compelled to lift, and Z_{es} of all altitudes below $CTHs$ perform the weakest with the smallest D_{ms} and lowest N_{ws} at corresponding altitudes and the lowest Ns of raindrops with different Ds at the ground. Afterwards, topographic forcing makes the dynamic and microphysical processes of the cloud and precipitation over the LP site more active and intense, and it can be found that both updrafts and downdrafts are enhancers. It is particularly noteworthy that V_{ts} , S_{ws} , and downward V_{as} concurrently and rapidly increase within the 0.6 km altitude above the ground over the LP site. Meanwhile, the larger Ds of the raindrops, as well as the higher Ns of small raindrops compared with LD and DW, facilitate the occurrence and dominance of the collision-coalescence process.

The probability distribution of radar variables, such as Z_{es} , V_{ts} , and V_{as} with heights, is relatively concentrated over the DW site, unlike LD and LP, which are more dispersed. The DW site is dominated by the downdrafts within all altitudes of the cloud precipitation, demonstrating again that the Liupan Mountains' topography has impacts on the dynamic structure of clouds and precipitation. Moreover, the values of V_{ts} over the DW site are always higher than those over LD and LP, and the faster V_{ts} drive surrounding air downward together. Meanwhile, the faster downdrafts themselves also drag raindrops down over the DW site, manifesting that there is a positive feedback mechanism between falling raindrops and downdrafts. The aforementioned phenomenon and mechanism can also be proved over LP in that both values of downward V_{as} and V_{ts} significantly increase near the ground. Overall, the research in this paper can provide a reference for the evaluation of operational sites and the precipitation efficiency of weather modification.

Author Contributions: Conceptualization, J.Z. and Z.S.; Methodology, Y.H. and X.J.; Software, J.Z.; Validation, Y.H. and X.J.; Formal analysis, Y.H.; Investigation, C.L.; Resources, Z.S.; Data curation, Y.Q.; Writing—original draft preparation, Y.H. and J.Z.; Writing—review and editing, J.Z. and C.L.; Visualization, Y.H.; Supervision, P.D. and T.L.; Project administration, X.Y. and Z.D.; Funding acquisition, Z.S., X.J. and Y.Q. All authors have read and agreed to the published version of the manuscript.

Funding: This research was funded by the National Natural Science Foundation of China (grant Nos. 42075073, 41975181), the Natural Science Foundation of Ningxia (grant No. 2021AAC03490) and the Postgraduate Research and Practice Innovation Program of Jiangsu Province in 2022 (grant No. KYCX22_1168).

Institutional Review Board Statement: Not applicable.

Informed Consent Statement: Not applicable.

Data Availability Statement: The data used herein is unavailable due to privacy.

Acknowledgments: We are grateful to the High-Performance Computing Center of Nanjing University of Information Science & Technology for their support of this work.

Conflicts of Interest: The authors declare no conflict of interest.

Appendix A

The electromagnetic wave of the Ka-band CR can be attenuated by the atmosphere, clouds, and precipitation during the propagation, which affects the acquired echo intensity and overall echo range of the observation. Therefore, an iterative procedure was used to correct the radar-measured Z_e . The procedure was based on the following relationships [69]:

$$k_i = \alpha Z_{correct}(i)^\beta,$$

$$\tau_i = \tau_{i-1} \times \exp(-2 \times k_i \times \Delta R),$$

$$Z_{correct}(i) = \frac{Z_e(i)}{\tau_{i-1}} \times \exp(k_i \times \Delta R),$$

where i represents the range gate number, k (dB km^{-1}) is the attenuation coefficient, τ (dB) is the two-way transmissivity, $Z_{correct}$ (dBZ) is the radar reflectivity after attenuation correction, and ΔR (m) is the radar gate length. Attenuation is a continuous process yielded from a near-to-far distance in the radar radial; therefore, the $Z_{correct}$ will be calculated gate-to-gate and the initial τ_0 and $Z_{correct}(0)$ was set to 1 and $Z_e(0)$, respectively. The coefficients α and β were set to 0.00334 and 0.73 according to the studies of Zheng et al. [29] and Matrosov et al. [70], respectively.

Table A1. List of abbreviations used in this paper.

No.	Abb.	Meaning	No.	Abb.	Meaning
1	CR	Ka-band millimeter-wave cloud radar	11	V	Raindrop falling velocity
2	MRR	K-band micro rain radar	12	CR	Combined reflectivity
3	OTT	OTT laser-based disdrometer	13	$Z_{correct}$	Radar reflectivity after attenuation correction
4	CTH	Cloud-top height	14	V_a	Vertical air velocity
5	R	Rain rate	15	D_m	Mass-weighted mean diameter
6	V_t	Particle falling velocity	16	N_w	Generalized intercept parameter
7	Z_e	Equivalent reflectivity factor	17	BB	Bright band
8	D	Raindrop diameter	18	σ_v	Standard deviation of rain rate
9	$N(D)$	Raindrop number concentration	19	Med	Median
10	S_W	Spectral width	20	Ave	Average

References

- Zhu, X.W.; Yang, J.L.; Cui, Y. Spatiotemporal distribution and formation causes of precipitation in the east of Northwest China during the period of 1961–2009. *Arid Zone Res.* **2013**, *30*, 1096–1099. (In Chinese)
- Zhang, P.; Yao, Z.Y.; Jia, S. Study of the characteristics of atmospheric water resources and hydrometeor precipitation efficiency over the Liupan Shan area. *J. Chin. J. Atmos. Sci.* **2020**, *44*, 421–434. (In Chinese)
- Houze, R.A. Orographic effects on precipitating clouds. *Rev. Geophys.* **2012**, *50*, RG1001. [CrossRef]
- Hu, L.; Deng, D.F.; Gao, S.T.; Xu, X.D. The seasonal variation of Tibetan convective systems Satellite observation. *J. Geophys. Res. Atmos.* **2016**, *121*, 5512–5525. [CrossRef]
- Wang, L.Z.; Miao, J.F.; Han, F.R. Overview of impact of topography on precipitation in China over last 10 years. *Meteorol. Sci. Technol.* **2018**, *46*, 12. (In Chinese)
- Li, J.J.; Zheng, J.F.; Liu, Y.X.; Cheng, Z.G.; He, J.S.; Ren, T.; Chen, S.J. A study on vertical structure and macro- to micro characteristics and differences of precipitation in Sichuan basin and the surrounding areas. *Acta. Meteorol. Sin.* **2022**, *80*, 205–223.
- Wang, Y.B.; Xie, X.H.; Meng, S.S.; Wu, D.D.; Chen, Y.C.; Jiang, F.X.; Zhu, B.W. Magnitude agreement, occurrence consistency, and elevation dependency of satellite-based precipitation products over the Tibetan Plateau. *Remote Sens.* **2020**, *12*, 1750. [CrossRef]
- Didlake, A.C.; Kumjian, M.R. Examining polarimetric radar observations of bulk microphysical structures and their relation to vortex kinematics in hurricane Arthur. *Mon. Weather Rev.* **2017**, *145*, 4521–4541. [CrossRef]
- Bachmann, K.; Keil, C.; Weissmann, M. Impact of radar data assimilation and orography on predictability of deep convection. *Q. J. R. Meteorol. Soc.* **2019**, *145*, 117–130. [CrossRef]
- Yan, Y.F.; Liu, Y.M. Vertical structures of convective and stratiform clouds in boreal summer over the Tibetan Plateau and its neighboring regions. *Adv. Atmos. Sci.* **2019**, *36*, 1089–1102. [CrossRef]
- Zhang, A.Q.; Fu, Y.F. Life cycle effects on the vertical structure of precipitation in east china measured by Himawari-8 and GPM DPR. *Mon. Weather Rev.* **2018**, *146*, 2183–2199. [CrossRef]

12. Lin, Y.L.; Reeves, H.D.; Chen, S.Y.; Chiao, S. Formation mechanisms for convection over the Ligurian Sea during MAP IOP-8. *Mon. Weather Rev.* **2005**, *133*, 2227–2245. [[CrossRef](#)]
13. Kirshbaum, D.J.; Bryan, G.H.; Rotunno, R.; Durran, D.R. The triggering of orographic rainbands by small-scale topography. *J. Atmos. Sci.* **2007**, *64*, 1530–1549. [[CrossRef](#)]
14. Lee, J.T.; Ko, K.Y.; Lee, D.I.; You, C.H.; Liou, Y.C. Enhancement of orographic precipitation in Jeju Island during the passage of Typhoon Khanun. *Atmos. Res.* **2018**, *201*, 58–71. [[CrossRef](#)]
15. Shao, Y.Y.; Liu, Q.J.; Jing, Z.J. Numerical simulation on macrophysics and microphysics structure of the orographic cloud and precipitation in summer of the Qilian Mountains. *J. Arid Meteorol.* **2013**, *31*, 18–23. (In Chinese)
16. Yu, X.J.; Zhao, Y. Simulation of Orographic effects on summer rain in the Tian Mountains. *J. Desert Res.* **2016**, *36*, 1133–1143. (In Chinese)
17. Cao, N.; Zhang, L.X.; Sang, J.R.; Yao, Z.Y.; Ma, N.; Tian, L. Observation and analysis on the macroscopic and microcosmic characteristics of topography, cloud and precipitation in Liupan Mountain area based on micro rain radar. *J. Meteorol. Sci.* **2019**, *39*, 775–785. (In Chinese)
18. Fu, Y.F.; Pan, X.; Xian, T. Precipitation characteristics over the steep slope of the Himalayas in rainy season observed by TRMM PR and VIRS. *Clim. Dyn.* **2018**, *51*, 1971–1989. [[CrossRef](#)]
19. He, J.S.; Zheng, J.F.; Zeng, Z.M.; Che, Y.Z.; Zheng, M.; Li, J.J. A comparative study on the vertical structures and microphysical properties of stratiform precipitation over south China and the Tibetan Plateau. *Remote Sens.* **2021**, *13*, 2897. [[CrossRef](#)]
20. Zhong, L.Z.; Chen, L.; Yang, R.F. Variability in the vertical structure of precipitation in Sichuan and Chongqing based on 2004–2014 space-borne observations. *Acta. Meteorol. Sin.* **2018**, *76*, 213–227. (In Chinese)
21. Luo, Y.L.; Zhang, R.H.; Qian, W.M. Intercomparison of deep convection over the Tibetan Plateau-Asian monsoon region and subtropical North America in Boreal summer using CloudSat/CALIPSO data. *J. Clim.* **2011**, *24*, 2164–2177. [[CrossRef](#)]
22. Deng, P.Y.; Mu, J.H.; Shu, Z.L.; Li, J.Y.; Tian, L.; Yang, Y. Analysis on the weather background and the macroscopic characteristics of cloud radar during the primary precipitation in Liupan Mountain area. *Ningxia Eng. Technol.* **2021**, *20*, 23–28. (In Chinese)
23. Wen, L.; Zhao, K.; Zhang, G.; Xue, M.; Zhou, B.; Liu, S.; Chen, X. Statistical characteristics of raindrop size distributions observed in East China during the Asian summer monsoon season using 2-D video disdrometer and micro rain data. *J. Geophys. Res. Atmos.* **2016**, *121*, 2265–2282. [[CrossRef](#)]
24. Wang, H.; Lei, H.C.; Yang, J.F. Microphysical processes of a stratiform precipitation event over eastern China: Analysis using micro rain radar data. *Adv. Atmos. Sci.* **2017**, *34*, 1472–1482. [[CrossRef](#)]
25. Peters, G.; Fischer, B.; Andersson, T. Rain observations with a vertically looking Micro Rain Radar (MRR). *Boreal Environ. Res.* **2002**, *7*, 353–362.
26. Peters, G.; Fischer, B.; Munster, H.; Clemens, M.; Wagner, A. Profiles of raindrop size distributions as retrieved by micro rain radars. *J. Appl. Meteorol.* **2005**, *44*, 1930–1949. [[CrossRef](#)]
27. Adirosi, E.; Baldini, L.; Roberto, N.; Gatlin, P.; Tokay, A. Improvement of vertical profiles of raindrop size distribution from micro rain radar using 2D video disdrometer measurements. *Atmos. Res.* **2016**, *169*, 404–415. [[CrossRef](#)]
28. Wen, L.; Zhao, K.; Wang, M.Y.; Zhang, G.F. Seasonal variations of observed raindrop size distribution in East China. *Adv. Atmos. Sci.* **2019**, *36*, 346–362. [[CrossRef](#)]
29. Zheng, J.F.; Zhang, P.W.; Liu, L.P.; Liu, Y.X.; Che, Y.Z. A study of vertical structures and microphysical characteristics of different convective cloud-precipitation types using Ka-Band millimeter wave radar measurements. *Remote Sens.* **2019**, *11*, 1810. [[CrossRef](#)]
30. Liu, L.P.; Zheng, J.F.; Ruan, Z.; Cui, Z.H.; Hu, Z.Q.; Wu, S.H.; Dai, G.Y.; Wu, Y.H. Comprehensive radar observations of clouds and precipitation over the Tibetan Plateau and preliminary analysis of cloud properties. *J. Meteorol. Res.* **2015**, *29*, 546–561. [[CrossRef](#)]
31. Liu, L.P.; Ruan, Z.; Zheng, J.F.; Gao, W.H. Comparing and merging observation data from Ka-band cloud radar, C-band frequency-modulated continuous wave radar and ceilometer systems. *Remote Sens.* **2017**, *9*, 1282. [[CrossRef](#)]
32. Liu, L.P.; Zheng, J.F.; Wu, J. A Ka-band solid-state transmitter cloud radar and data merging algorithm for its measurements. *Adv. Atmos. Sci.* **2017**, *34*, 545–558. [[CrossRef](#)]
33. Tokay, A.; Peterson, W.A.; Gatlin, P.; Wingo, M. Comparison of raindrop size distribution measurements by collocated disdrometers. *J. Atmos. Ocean. Technol.* **2013**, *30*, 1672–1690. [[CrossRef](#)]
34. Gossard, E.E.; Snider, J.B.; Clothiaux, E.E.; Martner, B.J.; Gibson, S.; Kropfli, R.A.; Frisch, A.S. The potential of 8-mm radars for remotely sensing cloud drop size distributions. *J. Atmos. Ocean. Technol.* **1997**, *13*, 76–87. [[CrossRef](#)]
35. Kollias, P.; Albrecht, B.A.; Lhermitte, R.; Savtchenko, A. Radar observations of updrafts, downdrafts, and turbulence in fair weather cumuli. *J. Atmos. Sci.* **2001**, *58*, 1750–1766. [[CrossRef](#)]
36. Ren, T.; Zheng, J.F.; Liu, L.P.; Zou, M.L.; Chen, S.J.; He, J.S.; Li, J.J. Retrieval of supercooled water in convective clouds over Nagqu of the Tibetan Plateau using millimeter-wave radar measurements. *J. Infrared Millim. Waves* **2022**, *41*, 831–843.
37. Chen, B.J.; Wang, J.; Gong, D.L. Raindrop size distribution in a midlatitude continental squall line measured by thies optical disdrometers over east China. *J. Appl. Meteorol. Climatol.* **2016**, *55*, 621–634. [[CrossRef](#)]
38. Das, S.K.; Konwar, M.; Chakravarty, K.; Deshpande, S.M. Raindrop size distribution of different cloud types over the Western Ghats using simultaneous measurements from Micro-Rain Radar and disdrometer. *Atmos. Res.* **2017**, *186*, 72–82. [[CrossRef](#)]
39. Janapati, J.; Seela, B.K.; Lin, P.L.; Lee, M.T.; Joseph, E. Microphysical features of typhoon and non-typhoon rainfall observed in Taiwan, an island in the northwestern Pacific. *Hydrol. Earth Syst. Sci.* **2021**, *25*, 4025–4040. [[CrossRef](#)]

40. Chen, B.; Hu, Z.; Liu, L.; Zhang, G. Raindrop size distribution measurements at 4,500 m on the Tibetan Plateau during TIPEX-III. *J. Geophys. Res. Atmos.* **2017**, *122*, 92–111. [[CrossRef](#)]
41. Battaglia, A.; Rustemeier, E.; Tokay, A.; Blahak, U.; Simmer, C. PARSIVEL snow observations: A critical assessment. *J. Atmos. Ocean. Technol.* **2010**, *27*, 333–344. [[CrossRef](#)]
42. Atlas, D.; Ulbrich, C.W. Path and area integrated rainfall measurement by microwave in the 1–3 cm band. *J. Appl. Meteorol.* **1977**, *16*, 1322–1331. [[CrossRef](#)]
43. Bringi, V.N.; Chandrasekar, V.; Hubbert, J. Raindrop size distribution in different climatic regimes from disdrometer and dual-polarized radar analysis. *J. Atmos. Sci.* **2003**, *60*, 354–365. [[CrossRef](#)]
44. Fabry, F.; Zawadzki, I. Long-term radar observations of the melting layer of precipitation and their interpretation. *J. Atmos. Sci.* **1995**, *52*, 838–851. [[CrossRef](#)]
45. Chen, B.; Yang, J.; Pu, J.P. Statistical characteristics of raindrop size distribution in the Meiyu Season observed in Eastern China. *J. Meteorol. Soc. Jpn.* **2013**, *91*, 215–227. [[CrossRef](#)]
46. Cha, J.-W.; Chang, K.-H.; Yum, S.S.; Choi, Y.-J. Comparison of the bright band characteristics measured by Micro Rain Radar (MRR) at a mountain and a coastal site in South Korea. *Adv. Atmos. Sci.* **2009**, *26*, 211–221. [[CrossRef](#)]
47. Yu, F.; Yao, Z.Y. Numerical study on the complex of the stratiform and embedded convective cloud precipitation: A case study. *Meteorol. Mon.* **2009**, *35*. (In Chinese)
48. Yuter, S.E.; Houze, R.A. Three-dimensional kinematic and microphysical evolution of Florida cumulonimbus Part II: Frequency distributions of vertical velocity, reflectivity, and differential reflectivity. *J. Mon. Weather Rev.* **1995**, *123*, 1941–1963. [[CrossRef](#)]
49. Fu, Y.F.; Lin, Y.H.; Liu, G.S. Seasonal characteristics of precipitation in 1998 over East Asia as derived from TRMM PR. *Adv. Atmos. Sci.* **2003**, *20*, 511–529.
50. Luo, Y.L.; Zhang, R.H.; Wang, H. Comparing occurrences and vertical structures of hydrometeors between Eastern China and the Indian monsoon region using CloudSat/CALIPSO data. *J. Clim.* **2009**, *22*, 1052–1064. [[CrossRef](#)]
51. Yuan, J.; Houze, R.A.; Heymsfield, A.J. Vertical structures of anvil clouds of tropical mesoscale convective systems observed by CloudSat. *J. Atmos. Sci.* **2011**, *68*, 1653–1674. [[CrossRef](#)]
52. Starzec, M.; Mullendore, G.L.; Kucera, P.A. Using radar reflectivity to evaluate the vertical structure of forecasted convection. *J. Appl. Meteorol. Climatol.* **2018**, *57*, 2835–2849. [[CrossRef](#)]
53. Wang, J.; Fan, J.; Houze, R.A.; Brodzik, S.R.; Zhang, K.; Zhang, G.J. Using radar observations to evaluate 3-d radar echo structure simulated by the energy exascale earth system model (E3SM) version 1. *Geoscientific Model Development* **2021**, *14*, 719–734. [[CrossRef](#)]
54. Yin, J.F.; Wang, D.H.; Zhai, G.Q. A study of cloud vertical profiles from the Cloudsat data over the East Asian Continent. *Acta Meteorol. Sin.* **2013**, *71*, 121–133. (In Chinese)
55. Zhang, Y.; Zhou, Q.; Lv, S.S. Elucidating cloud vertical structures based on three-year Ka-band cloud radar observations from Beijing, China. *Atmos. Res.* **2019**, *222*, 88–99. [[CrossRef](#)]
56. Sun, Y.T.; Dong, X.Q.; Cui, W.J. Vertical structures of typical Meiyu precipitation events retrieved from GPM-DPR. *J. Geophys. Res. Atmos.* **2020**, *125*, e2019JD031466. [[CrossRef](#)]
57. Wang, G.L.; Zhou, R.R.; Zhaxi, S.L.; Liu, S.N. Raindrop size distribution measurements on the Southeast Tibetan Plateau during the STEP project. *Atmos. Res.* **2021**, *249*, 105311. [[CrossRef](#)]
58. Du, S.; Wang, D.H.; Li, G.P. Analysis of the vertical structure of precipitation in south China based on dual-frequency spaceborne precipitation radar GPM product. *J. Trop. Meteorol.* **2020**, *36*, 115–130. (In Chinese)
59. Hobbs, P.V.; Easter, R.C.; Fraser, A.B. A theoretical study of the flow of air and fallout of solid precipitation over mountainous terrain. Part II: Microphysics. *J. Atmos. Sci.* **1973**, *30*, 813–823. [[CrossRef](#)]
60. Sumesh, R.K.; Resmi, E.A.; Unnikrishnan, C.K.; Jash, D.; Sreekanth, T.S.; Resmi, M.C.M.; Rajeevan, K.; Nita, S.; Ramachandran, K.K. Microphysical aspects of tropical rainfall during bright band events at mid and high-altitude regions over southern Western Ghats, India. *J. Atmos. Res.* **2019**, *227*, 178–197. [[CrossRef](#)]
61. Zhou, L.; Dong, X.; Fu, Z.; Wang, B.; Leng, L.; Xi, B.; Cui, C. Vertical distributions of raindrops and Z-R relationships using micro rain radar and 2-D-video disdrometer measurements during the Integrative Monsoon Frontal Rainfall Experiment (IMFRE). *J. Geophys. Res. Atmos.* **2019**, *125*, e2019JD031108.
62. Low, T.B.; List, R. Collision, coalescence and breakup of raindrops. Part I: Experimentally established coalescence efficiencies and fragment size distributions in breakup. *J. Atmos. Sci.* **1982**, *39*, 1591–1606. [[CrossRef](#)]
63. Huo, Z.Y.; Ruan, Z.; Wei, M. Statistical characteristics of raindrop size distribution in South China summer based on the vertical structure derived from VPR-CFMCW. *Atmos. Res.* **2019**, *222*, 47–61. [[CrossRef](#)]
64. Wu, Y.; Liu, L. Statistical characteristics of raindrop size distribution in the Tibetan Plateau and southern China. *Adv. Atmos. Sci.* **2017**, *34*, 727–736. [[CrossRef](#)]
65. Niu, S.; An, X.; San, J. Observational research on physical feature of summer raindrop size distribution under synoptic systems in Ningxia. *Plateau Meteorol.* **2002**, *21*, 37–44. (In Chinese)
66. Kumar, S.; Silva, Y. Vertical characteristics of radar reflectivity and DSD parameters in intense convective clouds over South East South Asia during the Indian summer monsoon: GPM observations. *Int. J. Remote Sens.* **2019**, *40*, 9604–9628. [[CrossRef](#)]
67. Wen, L.; Zhao, K.; Yang, Z.L. Microphysics of stratiform and convective precipitation during Meiyu season in Eastern China. *J. Geophys. Res. Atmos.* **2020**, *125*, e2020JD032677. [[CrossRef](#)]

68. Wen, L.; Zhao, K.; Zhang, G.F.; Liu, S.; Chen, G. Impacts of instrument limitations on estimated raindrop size distribution, radar parameters, and model microphysics during Mei-Yu Season in East China. *J. Atmos. Ocean. Technol.* **2017**, *34*, 1021–1037. [[CrossRef](#)]
69. Huang, X.Y.; Fan, Y.W.; Li, F.; Xiao, H.; Zhang, X. The attenuation correction for a 35GHz ground-based cloud radar. *J. Infrared Millim. Waves* **2013**, *32*, 325–330. (In Chinese) [[CrossRef](#)]
70. Matrosov, S.Y. Attenuation-based estimates of rainfall rates aloft with vertically pointing Ka-band radars. *J. Atmos. Ocean. Technol.* **2005**, *22*, 43–54. [[CrossRef](#)]

Disclaimer/Publisher’s Note: The statements, opinions and data contained in all publications are solely those of the individual author(s) and contributor(s) and not of MDPI and/or the editor(s). MDPI and/or the editor(s) disclaim responsibility for any injury to people or property resulting from any ideas, methods, instructions or products referred to in the content.